Microstructuring of 3D movie theater metallic screens to improve radiant intensity homogeneity and reduce crosstalk

Thomas Le Deun, Daniel Stoenescu, Jean-Louis de Bougrenet de La Tocnaye

Research Article | Vol. 29, No. 3 / 1 February 2021 / Optics Express 4308
Optics EXPRESS

Microstructuring of 3D movie theater metallic screens to improve radiant intensity homogeneity and reduce crosstalk

THOMAS LE DEUN,[1,2,*] DANIEL STOENESCU,[1] AND JEAN-LOUIS DE BOUGRENET DE LA TOCNAYE[1]

[1] IMT Atlantique, Optics Department, 655 Avenue du Technopole, 29280 Plouzane, France
[2] Eyes3shut, 305 Rue Claude Shannon, 29280 Plouzane, France
[*] thomas.ledeun@live.fr

Abstract: We present analytical and experimental results of the microstructuring of movie theater metallic screens. Our objective is to maintain the polarization state of reflected light and to control the distribution of light intensity avoiding hotspots. We derive analytical solutions of surface functions with an axial symmetry (kernel) that produces isotropic and Lambertian scattering. Then we model the diffraction that can occur with such kernels, ranging from a few microns to several hundred microns, and we give illustrations when illuminated by laser beams corresponding to future use of laser projectors. Finally, we discuss some of the challenges associated with the tiling of such kernels and their manufacturing.

1. Introduction

The principle of polarization multiplexing for 3D display applications has been known since at least 1923 [1]. It is mainly used in 3D movie theaters, and for other immersive applications such as Caves [2] or multiviewer displays [3,4]. Most commonly, two image channels are encoded with two orthogonal circular polarizers. The light is reflected on a screen and then the images are decoded with the left and right circular polarizers of the viewer's glasses. Compared to linear polarizers, it gives more freedom of movement to the viewer [5].

One of the main causes that affects visual comfort in 3D projection is related to the crosstalk ratio [6]. The crosstalk is defined in general as the leakage of the left or right image channel due to their incomplete isolation [7]. The crosstalk ratio is the ratio between the luminance through the blocking filter and the luminance through the passing filter. The crosstalk can create a visual effect called "ghosting", which can be described as the appearance of ghost images or double contours and which reduces the quality of the perceived image and can cause visual fatigue [8]. The main causes of crosstalk systems are the screen depolarization, the encoding and decoding technology and the movie theater geometry [9]. Conventional 'silver' screens are usually made of a matt white substrate of poly vinyl chloride (PVC) spray-painted with a mixture of resin binder and aluminium particles with random shape and size [10]. For systems with such conventional screens, the screen depolarization is the most critical factor responsible for the majority of crosstalk [11,12]. Coleman [10] distinguishes between true depolarization related to features smaller than the incoming wavelength (edge of the particles, surface roughness) and pseudo depolarization, related to multiple reflections on the surface.

In this paper we propose to reduce the depolarization thus we consider smooth surfaces that produce a single refection on the screen. While avoiding depolarization, we want to achieve more uniformity in the bidirectional reflectance distribution function (BRDF) so that, on the one hand each spectator can perceive the same brightness regardless of their position in the theater and on the other hand each viewer observes a more uniform image across the entire screen.

#408970 https://doi.org/10.1364/OE.408970
Journal © 2021 Received 1 Sep 2020; revised 12 Nov 2020; accepted 16 Nov 2020; published 27 Jan 2021

Optics EXPRESS

Numerous works have proposed surface models for computer graphics applications in order to determine the reflectance of objects [13,14]. Usually the bidirectional reflectance distribution function is computed by considering three different contributions: the ambient, specular and diffuse components. The ambient and diffuse components are commonly considered to reflect light equally in all directions, while the specular component depends on the location of the observer and the light source. Both diffuse and ambient light result from internal scattering or multiple reflections on the surface. Since to maintain the polarization state, multiple reflections are not acceptable, we must consider a surface that does not diffuse light. In addition, since applications of polarization-maintaining screens are usually located in dark rooms, ambient light can be neglected. Thus, we start this study with a purely geometrical approach to determine what surface profile could be used for such screen [15]. The surface is assumed to consist of micro-facets, each one of them being specularly reflective [16]. Since the surface kernels should be much smaller than the pixel size of the projected image (few millimeters at most), the diffraction effect cannot be neglected. Therefore we complete the geometrical approach analysis to take into account this effect and to match the experimental observations. This second approach considers the screen as an optical system that diffracts light because of the different optical paths introduced by the surface shape [17], in particular when the light source is a laser. The emergence of laser projectors makes this choice particularly relevant to analyze the light distribution reflected by the screen (including speckle). Finally, extension to non-coherent light source is done and illustrated showing the properties remain true.

2. Crosstalk induced by oblique incidence on a metal surface

Metallic screens have been used for passive 3D projection because it is simple to implement and relatively inexpensive [18]. Before we look for the surface profile that would satisfy a certain intensity distribution, we must evaluate the influence of the slope of the metal on the crosstalk ratio. Considering circular polarization, we can relate the Crosstalk Ratio (CR) to the Fresnel coefficients by simple modeling with Jones matrices.

$$CR = \frac{I_b}{I_p} = \left|\frac{1-\rho}{1+\rho}\right|^2, \quad \rho = r_{\parallel}/r_{\perp} \tag{1}$$

where I_b is the intensity through the blocking polarizer, I_p is the intensity through the passing polarizer, $r_{\parallel}$ and $r_{\perp}$ are the Fresnel coefficients on the reflective surface and ρ is the complex reflectance ratio. The complex reflectance ratio can be written as $\rho = \tan\Phi \exp(i\Delta)$, with $\tan\Phi$ the amplitude ratio upon reflection and Δ the phase shift difference. Trying to eliminate the crosstalk would therefore mean having $\rho = 1$, i.e. a zero phase difference and an amplitude ratio equal to one. This is only possible at normal incidence, so the crosstalk ratio should be evaluated over the incident angle. For a metal/air interface, the crosstalk ratio is given by:

$$CR = \left|\frac{\frac{\cos\theta_0}{\cos\theta_s} - \frac{\cos\theta_s}{\cos\theta_0}}{\frac{n_0}{n_s} - \frac{n_s}{n_0}}\right|^2 = \frac{n_0^2 \sin\theta_0^4}{\cos\theta_0^2 \left|n_0^2 \sin\theta_0^2 - n_s^2\right|} \tag{2}$$

where θ_0 is the angle of incidence on the metallic surface, n_0 the refractive index of the air, n_s the complex refractive index of the metal and $\theta_s = \arcsin(\frac{n_0}{n_s}\sin\theta_0)$. Equation (2) allows us to predict the crosstalk ratio and to compare different metals. In Fig. 1, the reflectance of the parallel and perpendicular components of the incoming electromagnetic wave to the plane of incidence, the phase shift and the crosstalk ratio have been drawn for silver (Ag), aluminium (Al) and gold (Au).

For all metals, the crosstalk is zero at normal incidence and then it rises with the angle of incidence. We can deduce from the graphs that the main contribution to the crosstalk is not the amplitude ratio upon reflection but the phase shift. Indeed, a phase shift introduced on an

Optics EXPRESS

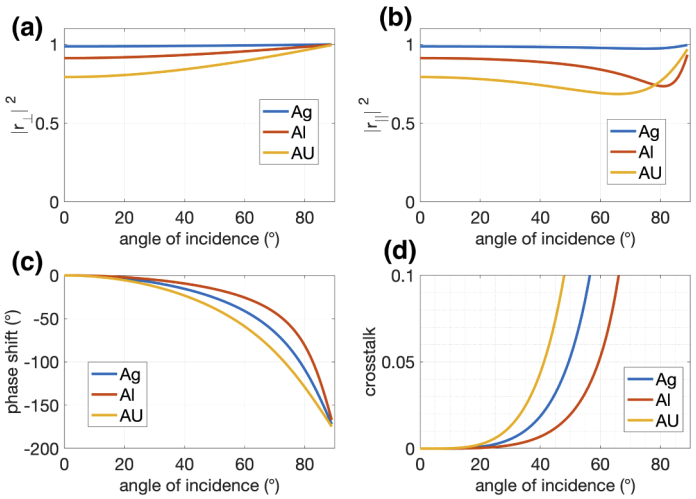

Fig. 1. Comparison of different metals for (a) perpendicular and (b) parallel Fresnel coefficients, (c) phase shift and (d) crosstalk ratio as a function on the angle of incidence, for $\lambda = 550$ nm.

incoming circular polarization will transform the circular polarization into an elliptical one. A metal with a higher imaginary part of its refractive index will produce less crosstalk. Here, Aluminium would be the best choice since the crosstalk is less than 1% for an angle of incidence of 40°.

It should be noted here that the crosstalk could be even further reduced by coating the metal with a thin film of dielectric material. In the case of a metal coated with a layer of refractive index n and thickness e, by computing the corresponding Fresnel coefficients, one can find the following crosstalk ratio:

$$CR = \left| \frac{\cos^2\varphi\left(\frac{\cos\theta_0}{\cos\theta_s} - \frac{\cos\theta_s}{\cos\theta_0}\right) + \sin^2\varphi\left(\frac{\cos^2\theta}{\cos\theta_s\cos\theta_0} - \frac{\cos\theta_s\cos\theta_0}{\cos^2\theta}\right) + i\frac{\sin(2\varphi)}{2}\left(\frac{n}{n_s} + \frac{n_s}{n}\right)\left(\frac{\cos\theta_0}{\cos\theta} - \frac{\cos\theta}{\cos\theta_0}\right)}{\cos^2\varphi\left(\frac{n_0}{n_s} - \frac{n_s}{n_0}\right) - \sin^2\varphi\left(\frac{n^2}{n_0 n_s} - \frac{n_0 n_s}{n^2}\right) + i\frac{\sin(2\varphi)}{2}\left(\frac{\cos\theta_s}{\cos\theta} + \frac{\cos\theta}{\cos\theta_s}\right)\left(\frac{n_0}{n} - \frac{n}{n_0}\right)} \right|^2 \tag{3}$$

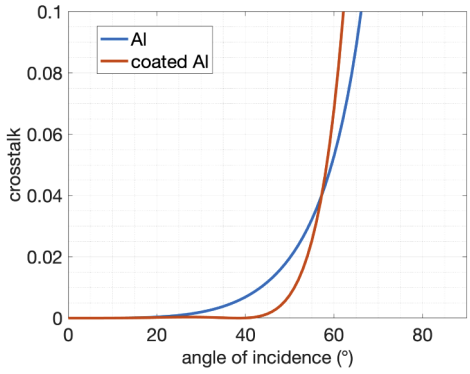

Fig. 2. Influence of the oblique incidence on the crosstalk ratio for a noncoated aluminium surface (blue line) and an aluminium surface coated with a layer of index $n = 1.4$ and thickness $e = 112$ nm for $\lambda = 550$ nm (red line)

Optics EXPRESS

where $\varphi = \frac{2\pi}{\lambda} ne$. From Eq. (3), we can numerically find that a dielectric layer of low refractive index (such as SiO_2 with $n \approx 1.4$) with a thickness of about a quarter-wave in optical thickness will produce better results as illustrated in Fig. 2.

The dielectric layer can serve at the same time as a protective layer against scratch and oxidation [11], but of course it will be more expensive. In all cases, such computations show that it is acceptable to have surfaces with slopes up to 40° (that is with maximum scattering angle up to 80°) while maintaining satisfactory level of crosstalk.

3. Analytical solutions based on a geometric approach

Here we consider the screen as a smooth structured metal surface, and look for a surface profile that would produce a given intensity distribution function. We consider an axially symmetrical surface profile $s(r)$ (kernel). On each point r of the screen, an incoming ray will be reflected specularly in relation to the slope $\theta_i(r)$ of the surface $s(r)$ on this point. Specifically, for an incoming ray at normal incidence, it will be reflected in the direction θ such that $\theta = 2\theta_i$ where θ_i correspond to the slope of the surface. The geometry and notations we use are shown in Fig. 3.

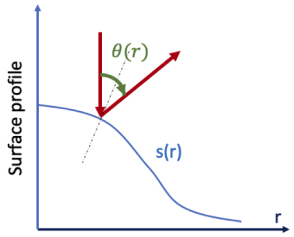

Fig. 3. Notations used for an axially symmetrical solution

Choosing the intensity distribution means finding which surface function $s(r)$ gives the corresponding function of intensity by steradian (radiant intensity). Looking for an axially symmetrical solution, the intensity by solid angle can be expressed as follow:

$$\text{Radiant intensity} = \frac{\text{Irradiance} \times \text{irradiated surface}}{\text{solid angle}} = \frac{E_0 2\pi r dr}{2\pi \sin\theta d\theta} = gD(\theta) \tag{4}$$

with E_0 the Irradiance, $D(\theta)$ the desired intensity distribution and g a constant (with respect to θ). 'g' can be computed by integrating Eq. (4). From Eq. (4), we can derive θ as a function of r. Then, the surface profile can be deduced by integrating the following equation:

$$ds/dr = \tan(\theta/2) \tag{5}$$

where $s(r)$ is the desired surface function. We call 'kernel' the surface produced by the rotation of the s function around the z axis. It is the fundamental building block of our screen.

3.1. Isotropic kernel

By definition, an isotropic diffuser has a constant intensity distribution function $D(\theta) = 1$. From Eq. (4), the following function $\theta(r)$ can be obtained:

$$\theta(r) = 2\arcsin(r/R_i) \tag{6}$$

with $R_i = \frac{r_m}{\sin(\theta_{max}/2)}$, r_m the maximum radius of the kernel and θ_{max} the maximum scattering angle desired. Using Eq. (5), the isotropic solution can be found:

$$s_i(r) = R_i\sqrt{1 - (r/R_i)^2} \tag{7}$$

Optics EXPRESS

It corresponds simply to a spherical cap, R_i is the scale factor of the kernel (and the radius of the corresponding sphere). The maximum scattering angle is simply obtained by choosing where the spherical cap ends.

3.2. Lambertian kernel

The intensity distribution that is sought more commonly for a screen is called Lambertian, and defines a screen where the apparent brightness is constant regardless of the observer's angle of view. The radiance of a Lambertian screen is constant while the radiant intensity obeys Lambert's cosine law [19]. With our notations, it corresponds to $D(\theta) = \cos(\theta)$. We want to have a constant radiance over a certain solid angle. In this case, a slightly different equation than in the isotropic case is found between θ and r:

$$\theta(r) = \arcsin(r/R_l) \tag{8}$$

where $R_l = \frac{r_m}{\sin(\theta_{max})}$. Integrating Eq. (5) using Eq. (8), we obtain the equation of the derivative of $s(r)$:

$$\frac{ds_l(r)}{dr} = \frac{1 - \sqrt{1 - (r/R_l)^2}}{r/R_l} \tag{9}$$

which has as a solution:

$$s_l(r) = R_l\{\ln(1 + \sqrt{1 - (r/R_l)^2}) - \sqrt{1 - (r/R_l)^2}\} \tag{10}$$

Computing the constant g in Eq. (4) as a function of the maximum scattering angle θ_{max} for a given kernel radius r_m, we find:

$$g(\theta_{max}) = \frac{2E_0 r_m^2}{1 - \cos(2\theta_{max})} \tag{11}$$

g is related to the gain G of the screen which is by definition the ratio between the intensity of a screen and the intensity of a Lambertian screen (with $\theta_{max} = \pi/2$) when illuminated at normal incidence. The relation between the gain and the maximum angle follows:

$$G(\theta_{max}) = \frac{g(\theta_{max})}{g(\pi/2)} = \frac{1}{\sin^2(\theta_{max})} \tag{12}$$

When we choose a maximum scattering angle smaller than $\pi/2$, the luminous intensity is distributed over a smaller solid angle, so the gain of the screen increases. It is advisable to clearly define the angular range necessary in order to choose the smallest maximum angle (θ_{max}) and thus increase the screen gain.

Figure 4 illustrates the difference between the isotropic and Lambertian kernels for a given maximum scattering angle. The maximum angle defines the slope at the end of the kernel. It can be seen that for an axially symmetrical kernel, the sign of the functions obtained is not important given the symmetry of the problem, the surface function and its opposite will both produce the same radiant intensity.

3.3. Managing the bidirectional reflectance distribution function

Managing the bidirectional reflectance distribution function BRDF is essential to make good use of the luminous intensity. Ideally each pixel, given the incident angle of the projector, should scatter the light only in the region where the spectators are seated, as illustrated in Fig. 5.

One way to control the BRDF, starting from a kernel able to distribute light uniformly, is to "cut out" that kernel, in a way which is related to the geometry of the theater. For instance, if we want light to be distributed only in the rectangular region of a movie theater where the spectators are seated, we keep only a rectangular part of the kernel.

Optics EXPRESS

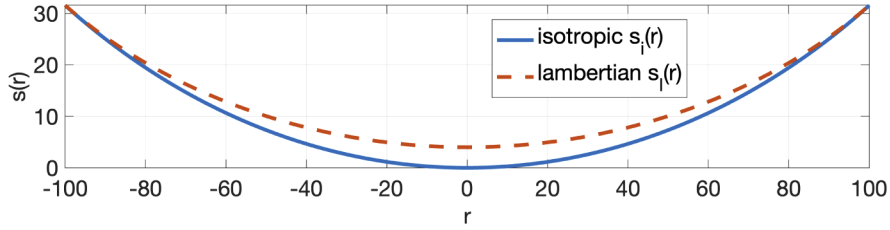

Fig. 4. Comparison between isotropic and Lambertian kernels for $\theta_{max} = 70°$

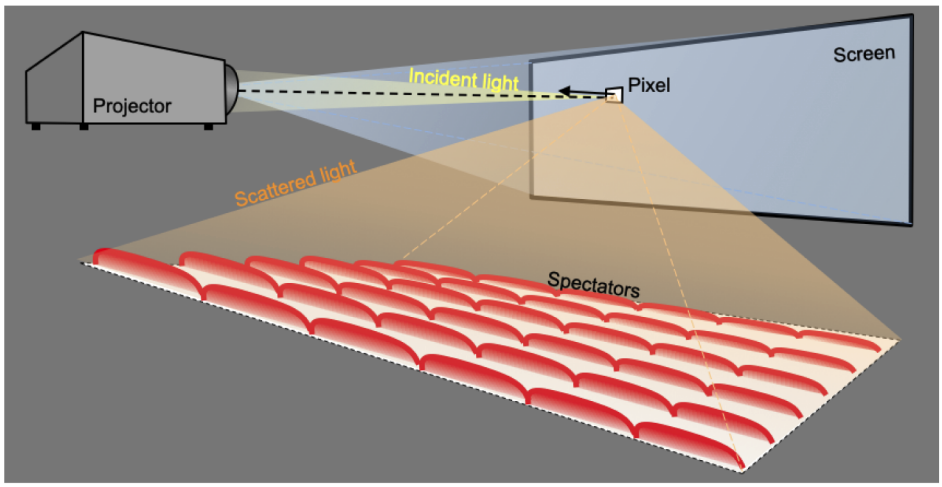

Fig. 5. Theater geometry and angles. The arrow represents the local normal direction to the screen surface

To illustrate this point we designed two gratings of Lambertian kernels, one with rectangular cut out kernels and the other with hexagonal kernels. The surface was shaped by parallell direct-write photolithography [20], with 30 μm kernels designed to scatter light with a maximum scattering angle of 60°. The surface is made reflective with a thin layer of gold ($\approx$ 100 nm). One way to visualize the BRDF is to illuminate the sample screen and observe its reflection on a second white screen. We illuminated both samples with a collimated Helium Neon laser beam (3 cm in diameter) at an angle of incidence of 15°, and the reflection is observed on a white screen placed at 15 cm from our samples. Both BRDF and their corresponding kernels geometry observed on an optical microscope are illustrated in Fig. 6.

The BRDF in Fig. 6 are not perfectly axially symmetrical because we are in oblique incidence. Both examples show that it is possible to control the shape of the BRDF. Here the samples have been designed to have a maximum scattering angle of 60° and it fits with experiment. The BRDF shape is controlled by cut off geometry of the kernels.

Optics EXPRESS

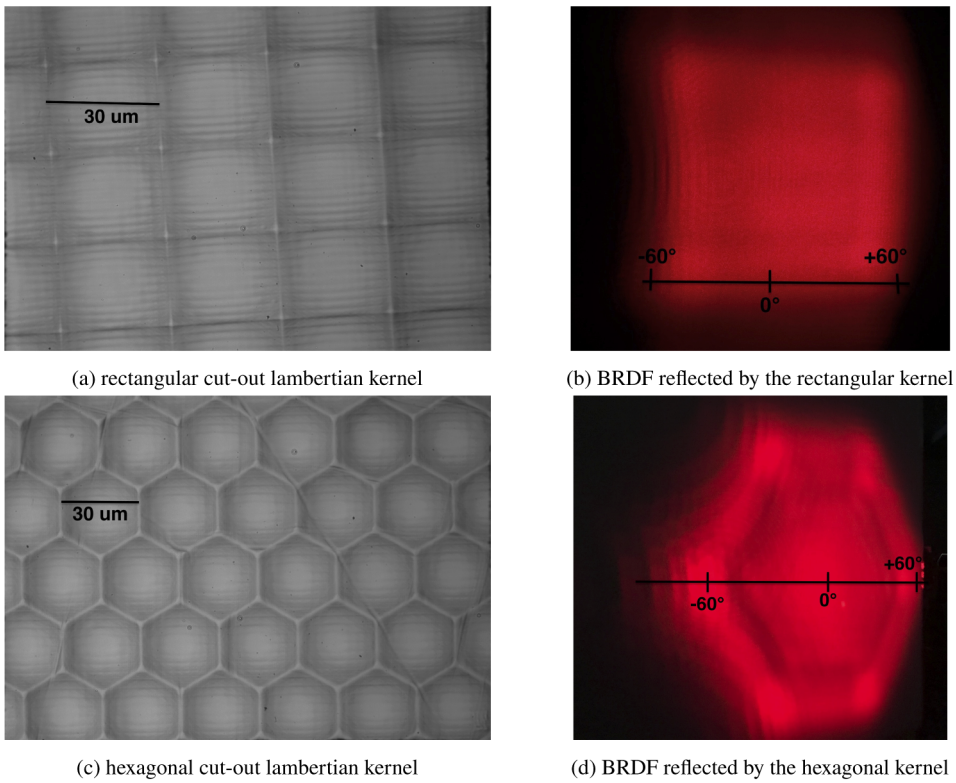

(a) rectangular cut-out lambertian kernel

(b) BRDF reflected by the rectangular kernel

(c) hexagonal cut-out lambertian kernel

(d) BRDF reflected by the hexagonal kernel

Fig. 6. Rectangular and hexagonal gratings and their corresponding BRDF geometry

4. Realization

In practice, to avoid alignment problems and Moire effects, the kernels should be smaller than a pixel displayed on the screen, so that a pixel covers several kernels. Such pixels are usually a few millimeters large. Ideally the basic kernel should not exceed 1 mm so that there is enough kernels in one pixel and that a small transverse offset of the pixel does not change significantly the radiant intensity. Moreover, they should be small enough that they are not resolvable by any viewer, that is smaller than a few hundreds microns. This raises two main challenges: one

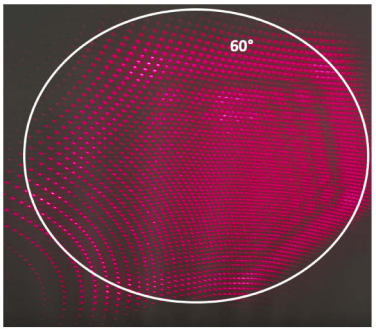

Fig. 7. Diffraction produced by hexagonal lattice, illuminated with a collimated He-Ne laser beam of 1 mm diameter and observed on a white screen at 30 cm

Optics EXPRESS

concerning how to pave the kernels on a 2D plane and the second concerning the impact of their size and the diffraction they induce.

From a purely geometric approach, the most natural way to tile an axially symmetrical kernel into a 2D space would be to form a hexagonal lattice. However, if the kernels are too small (typically between a few microns and several hundreds of microns) such lattice creates a diffracting grating. Figure 7 illustrates the diffraction produced with the grating of Fig. 6(c) when illuminated with a collimated laser beam (1 mm large) and observed at 50 cm. The luminance reflected on a screen is not constant. Instead, the light reflected from each of the kernels gives a multitude of coherent secondary sources that interfere strongly to create a 2D comb of intensity. However, the outer envelope of the light intensity distribution has the shape of the kernel, and the maximum angle can be controlled by its maximum slope. Thus, a pure geometrical modelling is not enough to the describe the phenomenon and diffraction should be considered.

4.1. Kernel-induced diffraction

To model the diffraction produced by one single kernel, which by construction distributes the light over wide angles, we use the nonparaxial scalar diffraction theory developed by Harvey and Krywonos [21]. Harvey has shown [22] that the diffracted radiance is a "fundamental quantity predicted by the Fourier transform of the optical disturbance emerging from a diffraction aperture, and [that] a paraxial limitation [is] not necessary in this linear systems formulation of wide-angle diffraction phenomena" [23]. The diffracted radiance can be written as follow:

$$L(\alpha, \beta - \beta_i) = K \cos\theta_i \lambda^2 / A_s \, |F\{U_0(\hat{x}, \hat{y}, 0) \exp(i2\pi\beta_i \hat{y})\}|^2 \tag{13}$$

where L is the radiant power per unit solid angle per unit projected area, U_0 is the complex amplitude distribution emerging from the diffracting aperture, λ the wavelength, A_s the area of the aperture, K a renormalization constant, $\hat{x}, \hat{y}$ the coordinates in the diffracting plane normalized by the wavelength ($\hat{x} = \frac{x}{\lambda}, \hat{y} = \frac{y}{\lambda}$), and α and β the direction cosines of the propagation vectors of the angular spectrum of plane waves discussed by Ratcliff [24], Goodman [25] and Gaskill [26].

The complex amplitude U_0 is calculated in relation to the optical phase difference $\Delta\phi$ introduced at each point of the surface $s(r)$ as follow [27]:

$$\Delta\Phi(r) = (\cos\theta_i + \cos\theta) s(r) \tag{14}$$

with $r = \sqrt{x^2 + y^2}$ $r \in [0, r_m]$ and θ_i the angle between the plane of the surface (xy) and the incoming beam.

This model allows us to predict the impact of the surface profile of a single kernel, of its size and of the maximum scattering angle. Its adequacy with experiments is shown in the following section 4.2.

4.1.1. Size of the kernel

First we modeled the impact of the size of the kernel, for a given maximum angle. In Fig. 8, it is clear that one single kernel produces a diffraction pattern, characterized by a number of fringes and their contrast. Smaller kernels produce fewer fringes with a larger contrast. Choosing the maximum slope allows us to control the maximum scattered angle, regardless of the size of the pattern. To obtain the best possible uniformity it is thus preferable to choose the largest possible radius.

4.1.2. Maximum scattering angle

With the simulations, we can also model the impact of the choice of the maximum scattering angle. As illustrated in Fig. 9, the number of fringes and their contrast are not affected by the maximum scattered angle. The average radiance decreases as the maximum angle increases,

Optics EXPRESS

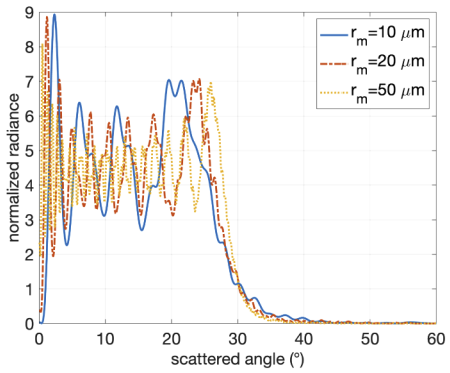

Fig. 8. Impact of the size of the kernel on the diffracted radiance, $\theta_{max} = 30°$

according to Eq. (12). This is due to the fact that the same irradiance is distributed over a larger solid angle.

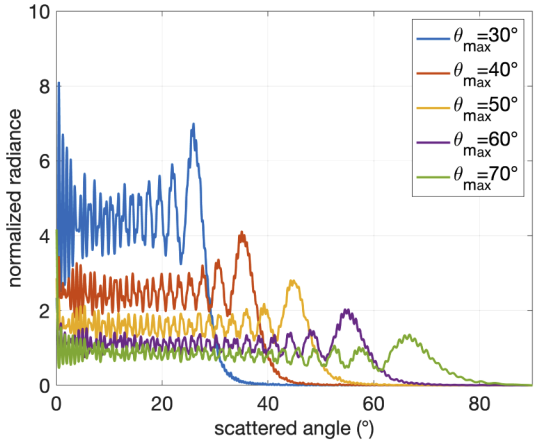

Fig. 9. Impact of the maximum scattering angle, $r_m = 50$ μm

4.1.3. Kernel pattern

Finally, the impact of different types of kernel can also be modeled. Different kernels will produce different surface slope distributions, affecting the optical phase difference in Eq. (14) and generating a different radiance. Figure 10 compares the isotropic and Lambertian kernels for a kernel with a radius of 100 μm.

While it is found that both kernels produce a radiance quite similar in terms of the fringes number, contrast and maximum angle, however, in the illuminated region, the radiance envelope is dictated by the kernel. The Lambertian kernel produces a more uniform radiance than the isotropic one. Moreover there is a gain increase with the Lambertian kernel related to the maximum scaterring angle, here the increase is about 20% for $\theta_{max} = 50°$. The relevance of the combined diffractive and geometrical approaches is thus confirmed, both of them being necessary to explain the diffracted radiance.

Optics EXPRESS

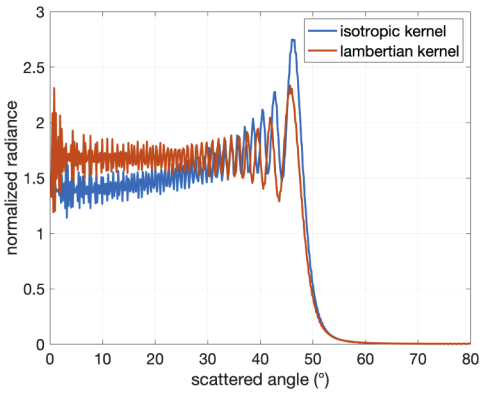

Fig. 10. impact of the kernel, $r_m = 100\ \mu$m, $\theta_{max} = 50°$

4.2. *Tiling-induced diffraction*

Since the diffracted radiance is associated to the Fourier transform of the complex amplitude induced by the kernel (see Eq. (13)), it is a linear system formulation that makes it easy to compute the overall diffraction produced by a set of patterns. For instance, it explains the results obtained with the hexagonal tiling in Fig. 7 since it is the convolution of the kernel with a 2D Dirac comb.

This linear formulation provides clues about how to tile the kernel. If we consider identical kernels with $r_m = 20\ \mu$m placed randomly on the surface, the radiance will be the product of the diffraction induced by the kernel and the diffraction induced by the random tiling. The overall diffraction will look like the kernel induced diffraction with some added noise as illustrated in Fig. 11. We observe some residual diffraction peaks that are due to the pixelization of our photo-plotter spatial light modulator creating parasitic gratings (as seen also in Figs. 12, 13 and 16). This parasitic grating is all the more visible as flat areas are left and the engraving depth is important. Since we left large flat surfaces (about 30%) on this sample, there is an intense specular reflection. This specular reflection can be eliminated by not leaving flat areas.

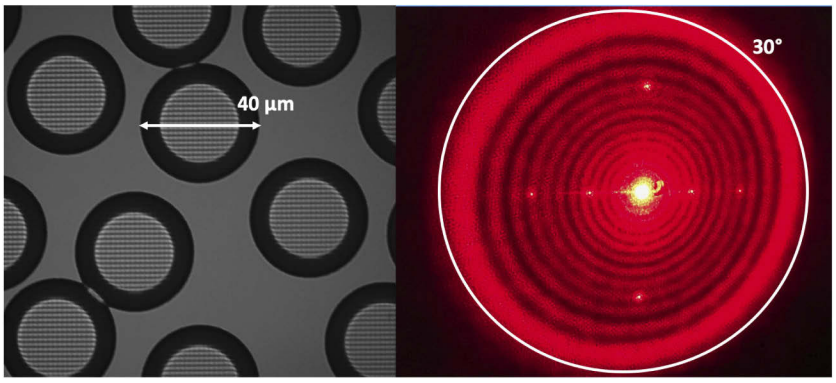

(a) randomly tiled kernels ($r_m = 20\ \mu$m) observed on an optical microscope

(b) Diffracted pattern produced by the randomly tiled kernels

Fig. 11. Random positions of a kernel

Optics EXPRESS

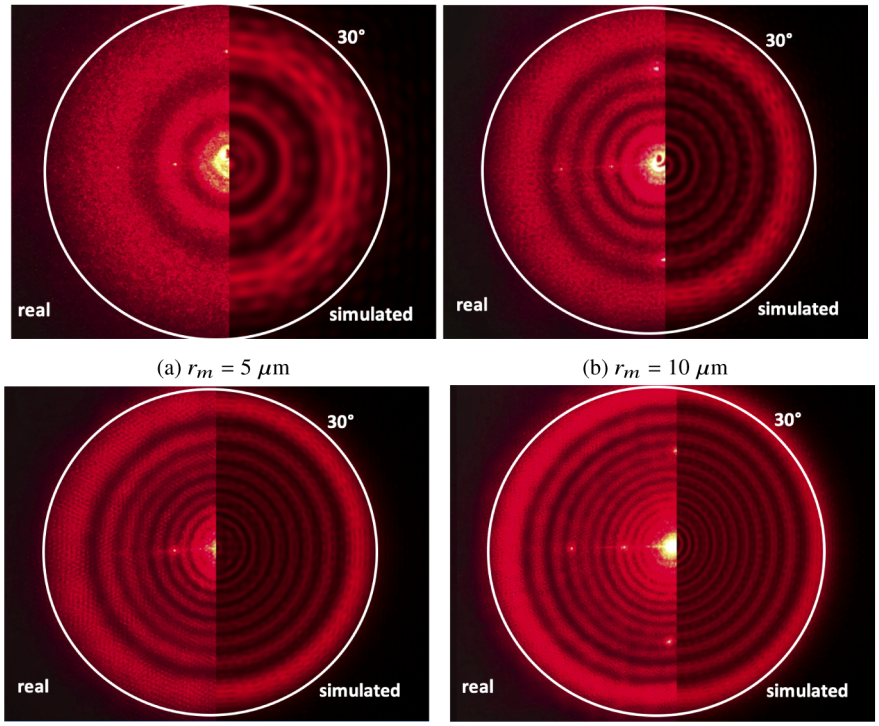

(a) $r_m = 5\ \mu$m (b) $r_m = 10\ \mu$m

(c) $r_m = 15\ \mu$m (d) $r_m = 20\ \mu$m

Fig. 12. Comparison between the experimental diffraction patterns (left) and simulated diffraction patterns (right) for $r_m = 5\ \mu$m (a), $r_m = 10\ \mu$m (b), $r_m = 15\ \mu$m (c) and $r_m = 20\ \mu$m

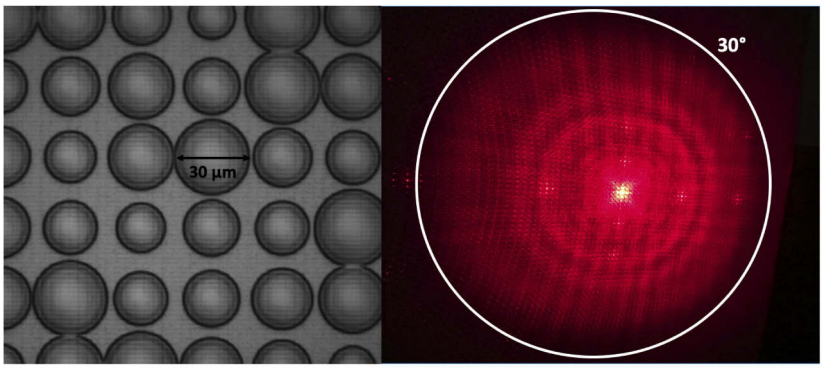

(a) regular lattice with random kernel size observed on an optical microscope

(b) Diffracted pattern produced by the random kernel size on a regular lattice

Fig. 13. Random kernel size on a regular lattice

Optics EXPRESS

To verify our theoretical model, we realized four samples made of randomly dispersed identical kernels of 10 μm, 20 μm, 30 μm and 40 μm. They are as previously illuminated by a collimated laser beam of 1 mm and the reflection of the sample is observed on a white screen placed at 30 cm. As illustrated in Fig. 12, the simulations predict the number and position of the fringes quite accurately.

The main difference between the experiments and the simulations is the central spot of the diffraction pattern. Naturally, the way we tiled the patterns left more or less flat reflective areas on the sample, creating a more or less intense peak in the specular area. Moreover, the real diffracted figures have a speckle like noise related to the way the kernels have been randomly tiled.

Since we aim at reducing the visibility of the fringes, one approach could be to tile a kernel with different radii regularly placed, in order to "mix" the different fringe patterns and reduce their contrast. Figure 13 shows that this approach reduces the visibility of the fringes.

While this approach also leaves large flat areas, a better way to tile the plane that both reduces the visibility of the fringes and fills the space as much as possible is to use randomization for both the position and diameter of the kernels, as illustrated in Fig. 14.

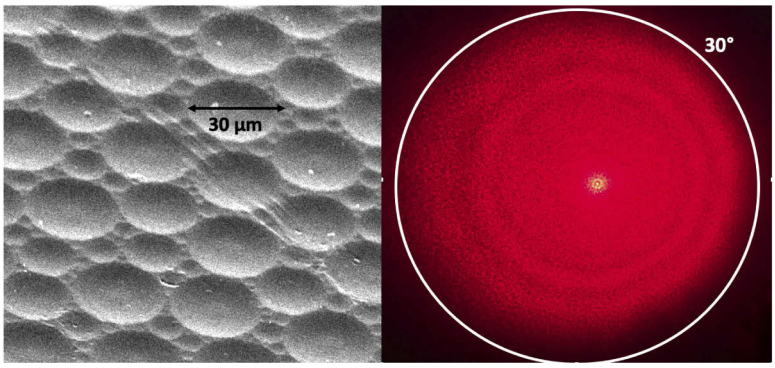

(a) Image of the random position and kernel size observed on scanning electron microscopy

(b) Scattering locus when (a) is illuminated with a 3 cm beam and observed on a screen at 25 cm

Fig. 14. Tiling with kernels of random sizes and positions

4.3. Noncoherent source

We have illuminated so far our samples with collimated coherent sources on 1 mm large surface in order to understand the diffraction phenomenon that appears and to be able to compare experiments and simulations. These conditions result in the appearance of strong interference effects. However in practice, the surface illuminated (one pixel) is a few millimeters large, and the spectral power distribution of a primary color has a width of more than 100 nm for non laser projectors. As illustrated in Fig. 15, a spatial (15b) or spectral (15c) broadening has quite the same effect of homogenizing the intensity distribution, and thus decreasing the visibility of the fringes.

This figure illustrates that the way we tested the diffraction patterns so far with a laser on a tiny surface (1 mm) corresponds to an extreme case (highly coherent) (Fig. 15) , but in real conditions, depending on the pixel size and the spectral width of the incoming light, the uniformity is improved (Fig. 15(b) and 15(c)).

Optics EXPRESS

4.4. Measured luminance

We measured the luminance as a function of the viewing angle with a luminance meters (Konica Minolta LS-100) for three samples illuminated by a 3 cm white spot from a BenQ projector at normal incidence. The luminance meter (1° acceptance angle), was placed at 60 cm and with viewing angles from 10° to 70°, to characterize the BRDF for a sample with random Lambertian kernels and a maximum scattering angle of 30° against a quasi Lambertian reference (white sheet of paper) and a conventional projection silver screen (ST Silver Screen from Screen-Tech).

From the measure of the irradiance on the screen (using an ILM 1335 luxmeter form ISO-TECH, $E_0 = 647 lm/m^2$), we can normalized the luminance so that 1 corresponds to the luminance of a Lambertian diffuser. In Fig. 16, naturally, the luminance of the quasi Lambertian reference is almost constant, while the conventional screen has a typical fast decreasing gain curve. In constrat, our screen sample has a quasi constant luminance over its scattering region and then drops drastically above 30° as expected.

4.5. Crosstalk

With the same measurement set-up as in section 4.4, we added blocking and passing circular polarizers in order to compute the crosstalk ratio for the same three samples for three different viewing angles. The results are depicted in Table 1.

The quasi Lambertian reference shows obviously a huge crosstalk ratio since it depolarizes the incoming light. Compared to the conventional screen, our sample with Lambertian kernels has

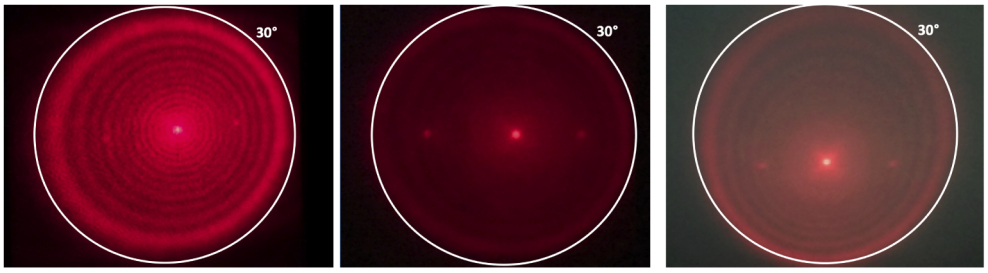

(a) coherent (b) spatial broadening (c) spectral broadening

Fig. 15. Screen sample with random size and position of Lambertian kernels illluminated with a collimated laser beam on a 1 mm wide surface (a), a collimated laser beam on a 3 mm wide surface (b) and a weakly converging beam from a typical red source from a BenQ projector ($\Delta\lambda \approx 120$ nm) (c)

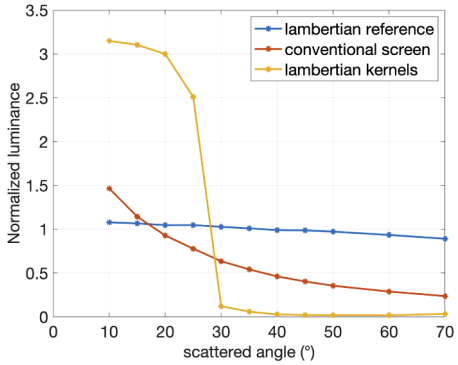

Fig. 16. Measured luminance as a function of the viewing angle

Optics EXPRESS

Table 1. Measured crosstalk ratio

	Lambertian reference	Conventional metallic screen	Random kernel sample
crosstalk ratio at 10°	0.80	0.046	0.0041
crosstalk ratio at 15°	0.92	0.053	0.0040
crosstalk ratio at 20°	1.00	0.064	0.0042

been able to reduce the crosstalk ratio by a factor of more than 10. Moreover, in contrast to the conventional screen, the crosstalk ratio does not depend on the viewing angle, which indicates that the main contribution to crosstalk is no longer the screen, but the extinction of the circular polarizers, which is 0.4%.

4.6. Visual comparison

To conclude, we propose a visual comparison between our screen with Lambertian kernels, the Lambertian reference (sheet of paper) and the conventional screen, in terms of luminance distribution and crosstalk. We put the three samples on the conventional screen, each has a size of 6 cm x 6 cm, the conventional screen is on the left, our sample in the middle and the Lambertian reference on the right, as shown in Fig. 17.

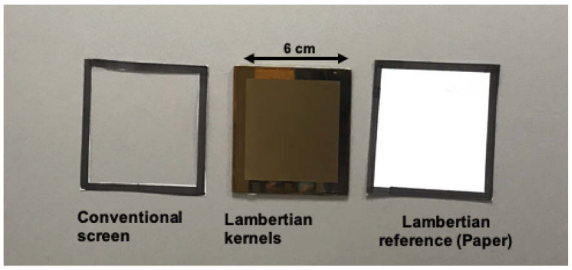

Fig. 17. Position of the three compared samples

Then we project an image (sea surface) on the three samples, and observe them from three different viewing angles, as shown in Fig. 18. Consistently with the results obtained in section 4.4, our sample is brighter at 5° and 25°, and appears almost perfectly dark at 45° (its maximum scattering angle is 30°).

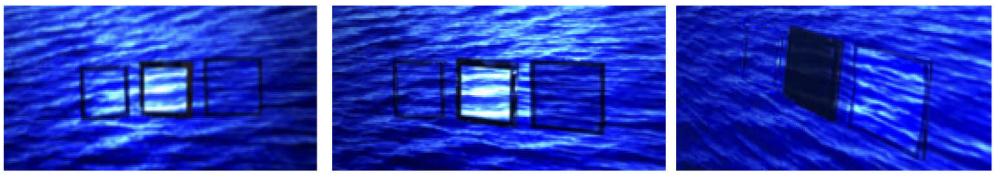

(a) 5° (b) 25° (c) 45°

Fig. 18. Photographs of the three samples observed from 3 different viewing angles

Similarly, we illustrate the good preservation of the polarization state. We show in Fig. 19 the three samples through the passing polarizing filters (left) and through the blocking polarizing filters (right).

Optics EXPRESS

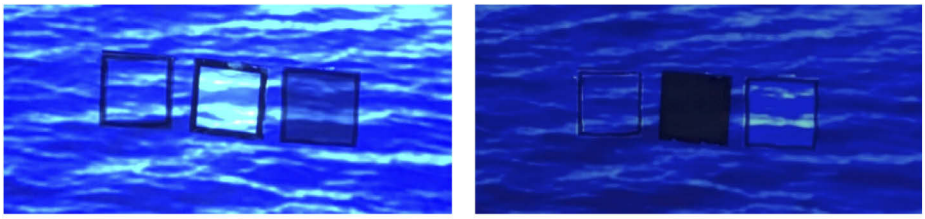

(a) Photograph through the passing polarizer

(b) Photograph through the blocking polarizer

Fig. 19. Observation of the three samples through (a) the passing filter and (b) the blocking filter.

5. Discussion

The diffractive model we used was able to predict accurately the diffraction patterns of our geometrical kernels when illuminated by coherent sources, which is in practice the worst case, since it creates interferences that affect the uniformity of the reflected radiance. This modeling is thus particularly appropriate to design screens for laser projectors. Conventional projectors have a wider power spectral density, which spreads the fringes and flattens the intensity curve. Broader-spectrum sources would also have a benefiting impact on the speckle like noise, due here to the randomization. Other speckle sources have not been considered because the metal surface is very smooth.

The main issue, we pointed out here, is the surface tiling to get rid of the residual specular reflection by minimizing (cancelling) the joining flat surfaces. As a solution, we have chosen to tile the 2D plane with kernels of different sizes, getting smaller and smaller in order to fill as much space as possible, while randomizing the position of the kernels. Our samples have a flat area representing less than 1% of the sample surface. This is the solution chosen but of course not optimal. Paving the space with aperiodic patterns is not an obvious task, deserving more attention. Suggestions could be found, for instance, in Voronoi diagrams [28], the challenge being to have a diversity of kernels while maintaining the overall radiance distribution. Another way is to accept the overlapping of neighboring kernels [11]. The impact of such overlapping should be studied carefully to maintain the overall radiance distribution.

Further investigations should be made to reduce the "hot spot", this small bright spot in the specular direction, that we observed even with almost no flat surfaces. This hot spot might be reduced by combining well chosen kernel sizes. Moreover, depending on the geometry of the theater, the hot spot can be sent outside the spectators regions. Indeed, by cutting the kernels accordingly, most of the intensity can be sent in another direction than the specular.

Funding

Association Nationale de la Recherche et de la Technologie (CIFRE 2017/0828).

Disclosures

TLD: Eyes3Shut (E)

References

1. L. Pictet and M. Cantoni, “Process and apparatus for the projection of stereoscopic kinematographic films,” (1925), CA253373A.
2. C. Cruz-Neira, D. J. Sandin, and T. A. DeFanti, “Surround-screen projection-based virtual reality: the design and implementation of the cave,” in *Proceedings of the 20th annual conference on Computer graphics and interactive techniques*, (1993), pp. 135–142.

Optics EXPRESS

3. V. N. H. Silva, D. Stoenescu, T. C. Nassour, J.-B. de la Riviere, and J.-L. de Bougrenet de la Tocnaye, "Ghosting impingements in 3d dual-view projection systems," J. Disp. Technol. **10**(7), 540–547 (2014).
4. A. Kulik, A. Kunert, S. Beck, R. Reichel, R. Blach, A. Zink, and B. Froehlich, "C1x6: a stereoscopic six-user display for co-located collaboration in shared virtual environments," ACM Trans. Graph. **30**(6), 1–12 (2011).
5. V. Walworth, S. Bennett, and G. Trapani, "Three-Dimensional Projection With Circular Polarizers," in *Optics in Entertainment II*, vol. 0462 (International Society for Optics and Photonics, 1984), pp. 64–70.
6. I. H. Marc, T. M. Lambooij, and Wijnand A. IJsselsteijn, "Visual discomfort in stereoscopic displays: a review," Proc. SPIE **6490**, 64900I (2007).
7. L. Lipton, "Factors Affecting Ghosting In Time-Multiplexed Piano-Stereoscopic Crt Display Systems," in *True Three-Dimensional Imaging Techniques & Display Technologies*, vol. 0761 (International Society for Optics and Photonics, 1987), pp. 75–79.
8. W. A. Ijsselsteijn, P. J. Seuntiëns, and L. M. Meesters, *Human Factors of 3D Displays* (John Wiley & Sons, 2005), chap. 12, pp. 217–233.
9. G. D. Sharp, D. Coleman, S. Gilman, and J. Chen, "54.1: Achieving high stereo-contrast-ratio in polarization-based 3d front projection," in *SID Symposium Digest of Technical Papers*, vol. 44 (Wiley Online Library, 2013), pp. 744–747.
10. D. Coleman and G. Sharp, "54.2: Invited paper: high efficiency polarization preserving cinema projection screens," in *SID Symposium Digest of Technical Papers*, vol. 44 (Wiley Online Library, 2013), pp. 748–751.
11. D. A. Coleman and G. D. Sharp, "Polarization preserving front projection screen," (2011). US Patent 7,898,734.
12. T. L. Deun, D. N. Stoenescu, and J.-L. de Bougrenet de la Tocnaye, "Effect of viewing directions in projection-based multiviewer display systems," Opt. Eng. **58**(10), 1–7 (2019).
13. R. L. Cook and K. E. Torrance, "A reflectance model for computer graphics," ACM Trans. Graph. **1**(1), 7–24 (1982).
14. B. T. Phong, "Illumination for computer generated pictures," Commun. ACM **18**(6), 311–317 (1975).
15. M. Piovarči, M. Wessely, M. Jagielski, M. Alexa, W. Matusik, and P. Didyk, "Directional screens," in *Proceedings of the 1st Annual ACM Symposium on Computational Fabrication*, (2017), pp. 1–10.
16. K. E. Torrance and E. M. Sparrow, "Theory for off-specular reflection from roughened surfaces," J. Opt. Soc. Am. **57**(9), 1105–1114 (1967).
17. P. Beckmann and A. Spizzichino, *The scattering of electromagnetic waves from rough surfaces* (Artech House, 1987).
18. "harkness," http://www.harkness-screens.com/.
19. J. H. Lambert, *Photometria sive de mensura et gradibus luminis, colorum et umbrae* (Klett, 1760).
20. M. M. Kessels, M. El Bouz, R. Pagan, and K. J. Heggarty, "Versatile stepper based maskless microlithography using a liquid crystal display for direct write of binary and multilevel microstructures," J. Micro/Nanolithogr., MEMS, MOEMS **6**(3), 033002 (2007).
21. J. E. Harvey and A. Krywonos, "A global view of diffraction: revisited," *Proc. SPIE AM100* 26 (2004).
22. J. E. Harvey and R. N. Pfisterer, "Understanding diffraction grating behavior: including conical diffraction and rayleigh anomalies from transmission gratings," Opt. Eng. **58**(08), 1 (2019).
23. J. Harvey, A. Krywonos, and C. L. Vernold, "Modified beckmann-kirchhoff scattering model for rough surfaces with large incident and scattering angles," Opt. Eng. **46**(7), 078002 (2007).
24. J. Ratcliffe, "Some aspects of diffraction theory and their application to the ionosphere," Rep. Prog. Phys. **19**(1), 306188 (1956).
25. J. W. Goodman, *Introduction to Fourier optics* (Roberts and Company Publishers, 2005).
26. J. D. Gaskill, *Linear systems, Fourier transforms, and optics*, vol. 576 (Wiley New York, 1978).
27. A. Krywonos, J. E. Harvey, and N. Choi, "Linear systems formulation of scattering theory for rough surfaces with arbitrary incident and scattering angles," J. Opt. Soc. Am. A **28**(6), 1121–1138 (2011).
28. F. Aurenhammer, "Voronoi diagrams a survey of a fundamental geometric data structure," ACM Comput. Surv. **23**(3), 345–405 (1991).